Fire Safety Journal 146 (2024) 104110

Contents lists available at ScienceDirect

Fire Safety Journal

journal homepage: www.elsevier.com/locate/firesaf

# Extinction coefficients from aerosol measurements

Christoph Gnendiger [a], Thorsten Schultze [b], Kristian Börger [a,c], Alexander Belt [a], Lukas Arnold [a,c,*]

[a] Institute for Advanced Simulation (IAS), Forschungszentrum Jülich, D-52428 Jülich, Germany
[b] Chair of Communication Systems (NTS), University of Duisburg–Essen, D-47057 Duisburg, Germany
[c] Chair of Computational Civil Engineering (CCE), University of Wuppertal, D-42119 Wuppertal, Germany

ARTICLE INFO

*Keywords:*
Visibility
Fire Dynamics
Light extinction
Light–particle interactions
Aerosol measurements
Classical electrodynamics
Civil-safety research
Computational fluid dynamics (CFD)

ABSTRACT

In this contribution, we develop a model that describes light extinction in the presence of arbitrary aerosols. In doing so, we take advantage of the fact that during measurements with the ELPI+-system, aerosol particles of any shape are internally mapped to spherical surrogates. The developed model is particularly simple and depends on only a few parameters, namely on densities and refractive indices of the measured aerosol particles. As proof of principle, the model is in first applications used to determine extinction coefficients and mass-specific extinction for an infrared light source with a peak wave length of 880 nm. Detailed studies concentrate on two aerosols exemplary for characteristic values of the input parameters: a paraffin aerosol in a bench-scale setup and soot from a flaming n-heptane fire in a room-scale setup (test fire TF5 according to EN54). As main results, we find values for mass-specific extinction that are different in the considered cases. Moreover, obtained results differ in part more than a factor of three from literature values typically used in practical applications. We explicitly assess reasons for deviations found and finally propose a simple way how future light-extinction studies can be performed comparatively easily using the ELPI+-system.

## 1. Introduction

Visibility in case of fire is an essential component in the performance-based safety design of buildings and therefore an indispensable aspect in the field of civil safety applications and research. Accordingly, a multitude of experiments investigating the human capacity to identify safety-relevant objects in the presence of soot has been conducted in the past, the first experiments dating back to the early 70s of the last century [1–5]. While the application field of the gained knowledge was initially limited to manual engineering procedures, it is nowadays also frequently applied in the field of computational fluid dynamics (CFD), for instance in the widely used *Fire Dynamics Simulator* FDS [6]. A reliable and comprehensive description of visibility in the presence of an aerosol has therefore become of central importance for the safety assessment of buildings and other places where people are present.

The key quantity to describe visibility in the context of environmental conditions is the *extinction coefficient* which quantifies properties of an aerosol to attenuate parts of a light beam from its original path. Conceptually, light extinction can be measured in two different ways: In a first approach, the focus is put on the light beam and the total amount of light-intensity reduction compared to the case without aerosol. Corresponding experiments are often called ‘direct’ visibility measurements and are usually evaluated using the Bouguer–Lambert law [7]. In contrast, in a second category of experiments, the focus is put on the aerosol instead and, for instance, quantities like number and mass densities, sizes, or even fractal properties of the constituting aerosol particles are measured. Using models that typically rely on Rayleigh or Mie computations and extensions thereof, visibility reduction is then deduced from the measured particle properties. Since in the latter approach visibility conditions are derived only in a downstream step and in the framework of the applied model, these measurements are sometimes denoted as ‘indirect’ ones.

To this day, there is considerable restraint and criticism regarding the ‘indirect’ approach. Objects of concern typically comprise the alleged presence of large experimental uncertainties [8,9] or the used models for light interaction of the aerosol particles [8–10]. Accordingly, many statements can be found in the literature claiming that ‘direct’ visibility measurements are the only reliable, or at least the preferable way to determine optical properties of aerosols [8–10]. An interesting quantity in this respect is the *mass-specific* extinction coefficient. Since it combines, by definition, light extinction with the overall mass density of the present aerosol, mass-specific extinction cannot be obtained through ‘direct’ visibility measurements alone but has always to be combined with other experimental results like gravimetric ones. In the literature, the existence of a (universal) mass-specific extinction coefficient has so far been investigated empirically, based on the hypothesis

* Corresponding author at: Institute for Advanced Simulation (IAS), Forschungszentrum Jülich, D-52428 Jülich, Germany.
*E-mail addresses:* arnold@uni-wuppertal.de, l.arnold@fz-juelich.de (L. Arnold).

https://doi.org/10.1016/j.firesaf.2024.104110
Received 4 July 2023; Received in revised form 22 December 2023; Accepted 3 February 2024
Available online 5 February 2024

that post-flame smoke produced by overventilated fires behaves almost identically and is more or less independent of the burned fuel (see for instance the review in [11] and references therein). Although functional dependences on different influencing factors like the wave length of the incident light [11] or the ventilation state of the fire [9] are qualitatively known, these aspects are often neglected for the sake of simplicity and, accordingly, the same constant value for mass-specific extinction is used in practical applications. FDS, for instance, uses by default the constant value proposed in [12] which itself is the review result of various small-scale experiments that have been conducted under well-controlled conditions. Given this fact, it is of major importance to know if universal mass-specific extinction does exist at all and, if so, to know its actual value in real-scale applications. Only then, it is possible to draw reliable conclusions that neither overestimate visibility conditions (which would be detrimental for safety aspects) nor underestimate them (which could result in unnecessary high expenses for safety measures).

In the present contribution, we therefore put the determination of (mass-specific) extinction on a firm basis by combining 'direct' and 'indirect' visibility measurements. More precisely, we combine aerosol measurements performed with the cascade impactor ELPI+ [13] and light-intensity reduction measurements performed with the extinction measuring equipment MIREX [14]. The goal of the comparison is to develop a practical model for the interaction of a light beam with aerosol particles that

- allows to reliably predict the total amount of light-intensity reduction in the presence of an arbitrary aerosol,
- is at the same time compatible with known value ranges of the entering model parameters,
- has expected predictive uncertainties comparable with 'direct' visibility measurements, and
- is preferably as simple as possible.

In order to achieve this, the structure of the paper is as follows: In Sections 2.1 and 2.2, we summarize key aspects of ELPI+- and MIREX-measurements in general and identify possible output of the two systems allowing to describe light extinction in a combined framework. Building on these findings, in Section 2.3 we develop a first-principle model that is based on classical electrodynamics and that fulfills the above requirements. In doing so, we explicitly assess all relevant assumptions made in the formulation of the model and discuss possible modifications that may (or may not) improve the predictive power in practical applications. In Section 3, we then apply the model and consider two different aerosols, namely paraffin and soot from flaming *n*-heptane fires which are exemplary for characteristic differences of the input variables. For the two cases, we determine value combinations of the model parameters which allow to bring ELPI+- and MIREX-measurements into the best possible agreement. This is done by explicitly computing extinction coefficients in Section 3.1 and mass-specific extinction in Section 3.2. Before concluding, in Section 3.3 we finally propose a simple methodology based on the developed model that allows to comparatively easily determine light extinction in future applications of the ELPI+-device.

## 2. Measuring and modeling light interaction with an aerosol

### 2.1. Aerosol measurements with ELPI+

The ELPI+-device is a cascade impactor which counts and classifies aerosol particles according to their aerodynamic and gravimetric properties [13]. Its working principle is as follows: In a first step, a sample of the aerosol under investigation is aspirated through a nozzle with an opening size of 10 µm and the contained aerosol particles are charged in a corona charger. For each electrically charged particle, the total amount of collected charge depends on the *surface area* of the particle and therefore indirectly on its size and shape. After charging, the aerosol sample is formed to a jet that successively passes 14 different impactor plates. Before passing each of the plates, the particles have to make a sharp turn, which for larger particles is not possible due to larger inertia. Accordingly, these particles are collected in the respective impactor plate and the arising electrical current $I(t)$ is measured. At the same time, smaller particles remain in the jet flow and move to the next impactor stage. Since the opening size of the device is decreasing from stage to stage, the speed of the jet flow is successively increasing, allowing also smaller particles to be collected. In this way, particles are collected and classified from larger to smaller size. The opening size of the lowest impactor stage is 0.006 µm.

As an output of an individual ELPI+-measurement one obtains in total 14 time-dependent electrical currents $I_i(t)$ with a time resolution of one second. Using conversion factors, measured currents can be converted into physical quantities like number densities $\rho_{\mathrm{N},i}$ and mass densities $\rho_{\mathrm{M},i}$ of the collected aerosol part [13]:

$$\rho_{\mathrm{N},i}(t) = \frac{N_i(t)}{V_\mathrm{u}} = X_{N_i} \cdot I_i(t)\,, \qquad i \in \{1,\dots,14\}\,, \tag{1a}$$

$$\rho_{\mathrm{M},i}(t) = \frac{M_i(t)}{V_\mathrm{u}} = \rho_{\mathrm{N},i}(t) \cdot \left(\pi \frac{d_{\mathrm{S},i}^3}{6}\right) \cdot \rho_{\mathrm{part},i}\,, \qquad i \in \{1,\dots,14\}\,. \tag{1b}$$

By convention, the ordering of the channel labels is such that $i = 1$ denotes the ELPI+-channel collecting the smallest particles, whereas $i = 14$ corresponds to the channel collecting the largest particles. In Eqs. (1), $N_i$ and $M_i$ denote absolute particle numbers and particle masses per unit volume $V_\mathrm{u} = 1\,\mathrm{cm}^3$ of the measured aerosol and the conversion factors $X_{N_i}$ consider charging and collection inefficiencies of the ELPI+-device. The latter are calibrated in [15] and provided in Appendix A.1 for the sake of completeness. Explicit definitions of $d_{\mathrm{S},i}$ and $\rho_{\mathrm{part},i}$ are given in the next paragraph.

A crucial point in the evaluation of ELPI+-data is that each of the 14 measured currents $I_i$ (and therefore each of the derived densities) can be assigned a dedicated particle size which is directly related to aerodynamic and gravimetric properties of the collected particles. For that, each (irregularly shaped) aerosol particle is internally converted into a virtual *equivalent particle* which is spherical and which has the same settling velocity $v_s$ as the actual aerosol particle. While the settling velocity of the aerosol particle is indirectly measured by the ELPI+-device, it is for the virtual equivalent particle given by Stoke's law, i. e.

$$v_s = \frac{g}{18\,\mu_\mathrm{air}}(\rho - \rho_\mathrm{air}) \cdot d^2\,. \tag{2}$$

Here, $g \approx 9.81\,\mathrm{m\,s^{-2}}$ is the standard acceleration due to gravity, $\mu_\mathrm{air} \approx 1.8 \cdot 10^{-5}\,\mathrm{kg\,m^{-1}\,s^{-1}}$ and $\rho_\mathrm{air} \approx 1.2\,\mathrm{kg\,m^{-3}}$ are the dynamic viscosity and mass density of air at a given temperature, respectively. The three quantities are related to measuring conditions of the experiments and are approximately the same for each individual ELPI+-measurement.[1] In contrast, $\rho$ and $d$ denote the mass density and the diameter of the equivalent particle, respectively. The two quantities therefore strongly depend on the measured aerosol. For a given settling velocity, there are two common ways to *define* the diameter of the equivalent sphere, see also Fig. 1:

(1) **Stokes equivalent diameter** $d_\mathrm{S}$
In this case, the diameter of the equivalent particle is defined such that the latter has the same settling velocity and the same particle density $\rho_\mathrm{part}$ as the real aerosol particle:

$$v_s =: \frac{g}{18\,\mu_\mathrm{air}}(\rho_\mathrm{part} - \rho_\mathrm{air}) \cdot d_\mathrm{S}^2\,. \tag{3a}$$

[1] Of course, $g$, $\mu_\mathrm{air}$, and $\rho_\mathrm{air}$ are affected by various boundary conditions of the experiments like ambient temperature or height above sea level. Compared to other sources of uncertainty, however, these factors can be regarded negligible, as will be shown below.

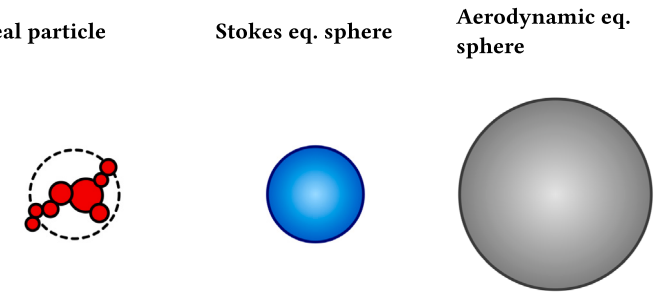


**Fig. 1. Possible definitions of the equivalent diameter.** In both cases, the irregularly shaped (aerosol) particle is mapped to a spherical surrogate. The diameter of the respective sphere is an output of the measuring device and can be used for further evaluation. The figure is adopted from the ELPI+-manual [13].

(2) **Aerodynamic equivalent diameter** $d_{\text{aero}}$
In this case, the diameter of the equivalent particle is defined such that the latter has the same settling velocity as the real aerosol particle. However, the equivalent particle is assumed to have unit density, i. e. $\rho = 1\,\text{g}\,\text{cm}^{-3}$:

$$v_s =: \frac{g}{18\,\mu_{\text{air}}}(1\,\text{g}\,\text{cm}^{-3} - \rho_{\text{air}}) \cdot d_{\text{aero}}^2\,. \tag{3b}$$

It should be noted that both definitions introduce auxiliary objects that may differ from the actual size of the initial aerosol particle. For instance, setting equal both definitions in Eqs. (3) and neglecting the density of air, it is straightforward to derive the following relation[2]:

$$\frac{d_{\text{S}}}{d_{\text{aero}}} \approx \sqrt{\frac{1\,\text{g}\,\text{cm}^{-3}}{\rho_{\text{part}}}}\,. \tag{4}$$

Accordingly, in case the actual particle density $\rho_{\text{part}}$ is larger (smaller) than $\rho = 1\,\text{g}\,\text{cm}^{-3}$, aerodynamic diameters are larger (smaller) than corresponding Stokes diameters. Since an exemplary particle density of $\rho_{\text{part}} = 4\,\text{g}\,\text{cm}^{-3}$ is assumed in Fig. 1, for instance, the diameter of the aerodynamic equivalent sphere is twice as large as the diameter of the corresponding Stokes sphere and therefore much larger than the size of the real aerosol particle. In contrast, the given Stokes equivalent diameter is compatible with the geometrical size of the irregularly shaped aerosol particle since it considers one additional physical property, namely the density $\rho_{\text{part}}$ of the aerosol particle. In order to get equivalent diameters that are close to the geometries of the aerosol particles, therefore Definition (3a) should be used instead of (3b). In Appendix A.3 we further investigate differences between both approaches and explicitly quantify the impact of the choice on obtained numerical results. At this point it remains to be mentioned that, since $\rho_{\text{part}}$ is not measured by the ELPI+-device, its value has either to be measured separately or to be taken from the literature.

Introducing Stokes equivalent spheres via Eq. (3a) allows to assign dedicated particle diameters to each of the 14 measured currents $I_i(t)$ of an ELPI+-experiment, as mentioned before:

$$I_i(t) \;\leftrightarrow\; d_{\text{S},i}(\rho_{\text{part},i})\,, \qquad i \in \{1, \dots, 14\}\,. \tag{5}$$

The quantities $d_{\text{S},i}$ and $\rho_{\text{part},i}$ denote the geometric mean of the Stokes equivalent diameters and the particle density associated with ELPI+-stage $i$, respectively. In Section 3, these combinations of measured electrical currents and deduced diameters are used to compute extinction coefficients of different aerosols.

*Aerosol density* $\rho_{\text{aerosol}}$

An important quantity the total amount of light extinction depends on is the overall mass density $\rho_{\text{aerosol}}$ of the aerosol. One advantage of ELPI+-measurements in general is that the quantity can be deduced from obtained experimental data. This is done by summing up particle masses measured by the different ELPI+-stages and normalizing to unit volume, as done e. g. in Eq. (1b). Considering the first $n$ ELPI+-stages, for example, the density of the corresponding aerosol part is given by

$$\rho_{\text{aerosol}}^{(n)}(t) := \sum_{i=1}^{n} \rho_{\text{M},i}(t)\,, \qquad n \in \{1, \dots, 14\}\,. \tag{6}$$

In the considered setup, each $\rho_{\text{aerosol}}^{(n)}$ is mainly governed by the particle densities $\rho_{\text{part},i}$. This dependence, however, is only weak. The reason is that individual mass concentrations $\rho_{\text{M},i}$ are determined indirectly from volumes and mass densities of the Stokes equivalent particles, see Eq. (1b). Since an increase of the particle density at the same time corresponds to smaller Stokes equivalent diameters and therefore to smaller volumes, both effects compensate each other and result in a weak dependence on the actual value of $\rho_{\text{part},i}$. In other words, obtained values for $\rho_{\text{aerosol}}^{(n)}$ are approximately a direct output of an ELPI+-measurement as a consequence of internal conversion processes.[3]

*Average distance between aerosol particles*

A quantity closely related to the aerosol density is the average distance $\bar{l}_d$ between the aerosol particles. It can be obtained via dividing

[2] Actually, the functional dependence on the value of $\rho_{\text{part}}$ is slightly more complicated and even depends on the respective ELPI+-channel, see in particular the ELPI+-manual [13]. However, Eq. (4) serves as a useful approximation for the present considerations.

[3] Overall, ELPI+ conversion factors for mass density are proportional to $\rho_M \propto \rho_{\text{part},i} \cdot (d_{\text{S}})^{3-a}$ with $a \in \{1.225, 1.515, 1.085\}$, depending on the respective Stokes equivalent diameter, see Eq. (1b) and Eqs. (24) in Appendix A.1. Stokes equivalent diameters in turn are proportional to $d_{\text{S}} \propto (\rho_{\text{part},i})^{-\frac{1}{2}}$ which can be seen in Eq. (4). In total, conversion factors are therefore proportional to $\rho_M \propto (\rho_{\text{part},i})^{\frac{a-1}{2}}$ with a maximum dependence given by $\rho_M \propto (\rho_{\text{part},i})^{\frac{1.515-1}{2}} = (\rho_{\text{part},i})^{0.2575}$. Doubling $\rho_{\text{part},i}$, for example, then only leads to a mass concentration increase of at most 20%. In practice, the increase is typically much smaller in the order of a few percent, which is shown in Section 3.

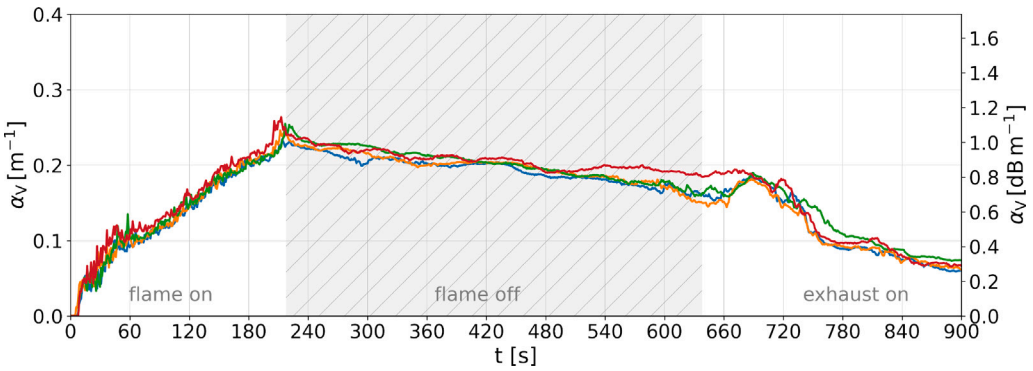


**Fig. 2. Time-dependent light extinction measured by the MIREX-system.** Shown are results for soot from flaming *n*-heptane fires obtained in four independent experiments. Details of the experimental setup are provided in Section 3.

the unit volume $V_u$ by the absolute particle number $N_u$ present in that volume,

$$\bar{l}_d^{-3} = \frac{V_u}{N_u} = \frac{1\,\mathrm{cm}^3}{N_u}\,. \tag{7}$$

As it turns out, in the experiments conducted in this contribution, the maximum particle number within the steady states is $N_u \approx 5 \cdot 10^6$, resulting in a minimal distance of $\bar{l}_d \approx 60\,\mu\mathrm{m}$. Accordingly, the average distance between the aerosol particles is much larger than the size of the equivalent spheres which is (much) smaller than $d_S = 10\,\mu\mathrm{m}$. Aerosol particles can therefore be assumed to interact independently of each other and only with the incoming light beam in terms of single-particle interactions [7].

### 2.2. Transition measurements with MIREX

As a second, independent measuring system for light interaction of aerosol particles we use the well-established extinction measuring equipment MIREX [14]. The device analyzes smoke densities based on optical measurements in the infrared domain of the spectrum. More precisely, the system uses pulsed light from a diode as light source and sends it to a reflecting mirror in approximately one meter distance from the emitter. The reflected light is then measured by a receiver, resulting in an overall length of the optical path of $l = 2\,\mathrm{m}$. Accordingly, the MIREX constantly measures light-intensity reduction in an area of one meter extension. The specification of the light spectrum is such that the main part of the power is emitted in the wave length range between $0.8\,\mu\mathrm{m}$ and $0.95\,\mu\mathrm{m}$. The peak wave length of the distribution is $\lambda_{in} \approx 0.88\,\mu\mathrm{m}$.

As an output of an individual MIREX-measurement, one obtains time-dependent values for the (volume) extinction coefficient $\alpha_V$ that enters the Bouguer–Lambert law [7]

$$\frac{I(t)}{I_0} = e^{-\alpha_V(t)\cdot l}\,. \tag{8}$$

Here, $I(t)$ is the measured time-dependent light intensity and $I_0$ is the intensity of the light source without aerosol. Sample output of the conducted experiments is shown in Fig. 2.

### 2.3. Light extinction in classical electrodynamics

One main goal of the present contribution is to describe light extinction in the presence of different aerosols by using ELPI+-measurements (discussed in Section 2.1) and MIREX measurements (discussed in Section 2.2). In the following, we provide theoretical background that is necessary to evaluate ELPI+-data accordingly. Our approach is the following: In a first step, we start with a basic theory that is as simple as possible but covers, nevertheless, all relevant aspects of the underlying physical processes. Then, we discuss possible modifications of the theory that may (or may not) improve the predictive power of the initial model.

In a first-order approach, the interaction of a light beam with a spatially extended aerosol is an electrodynamic process that can be adequately described by classical electrodynamics where relativistic and quantum effects are neglected. Moreover, to obtain meaningful results in the context of the present work, we make the following additional assumptions:

- In Section 2.1 it is shown that the ELPI+-device assigns dedicated Stokes equivalent diameters $d_S$ to each of the 14 measuring channels. In the following, we therefore assume aerosol particles to optically behave like **homogeneous spheres**, each with an individual geometrical diameter $d_{geom} \equiv d_S$ and refractive index $m$. All particles are considered to be monodisperse and to interact independently of each other in terms of single-particle interactions.
- In Section 2.2 it is mentioned that the intensity distribution of the MIREX light source is comparatively narrow. In the following, we therefore assume the incident light beam to consist of **plane, unpolarized**, and **monochromatic electromagnetic waves**. As wave length $\lambda_{in}$ we take the peak wave length of the intensity distribution which is in the infrared and given by $\lambda_{in} = 0.88\,\mu\mathrm{m}$.

Of course, these assumptions only represent a first-order description of the optical effects actually taking place. We show, however, that even with these strong restrictions it is possible to obtain reliable numerical results under various different conditions. In order to show this, we explicitly determine the following quantities:

*Extinction efficiency* $q_{ext}$

This parameter quantifies the ability of a single particle to attenuate parts of a light beam from its original path. Starting from Maxwell's equations, it can be computed from basic principles and contains the two major components *scattering* and *absorption* [7]:

$$q_{ext} = q_{sca} + q_{abs} = q_{ext}(\lambda_{in}, d_S, m)\,. \tag{9}$$

Absorption is not present for every aerosol and governed by the imaginary part of the refractive index $m$. Moreover, extinction efficiency depends on the wave length $\lambda_{in}$ of the incident light as well as on the equivalent diameter $d_S$ of the interacting particle. It can be computed e. g. by using the freely available software *MiePlot* [16] which itself is based on the code published in the appendix of [7]. Sample output of the software for two different refractive indices is shown in Fig. 3. As can be seen, the measuring range of the ELPI+-device, which ranges from $0.006\,\mu\mathrm{m}$ to $10\,\mu\mathrm{m}$ [13], covers the global maximum of the efficiency distributions, respectively.

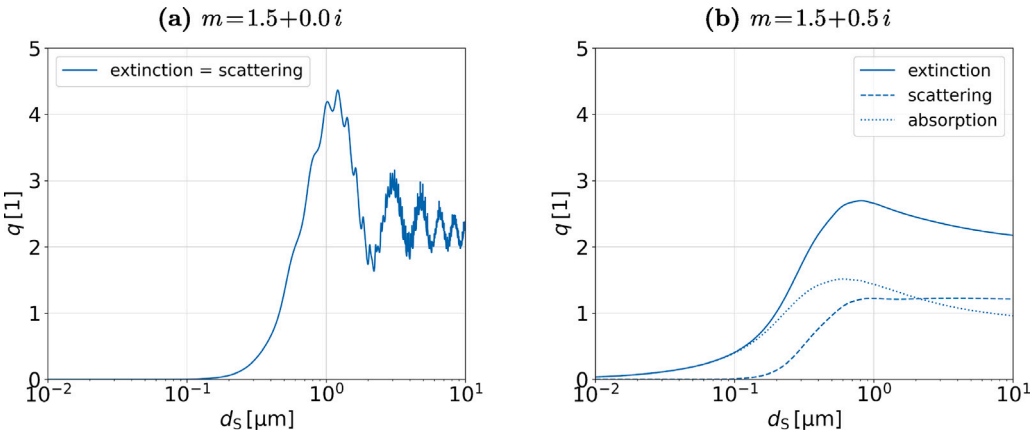


**Fig. 3. Extinction efficiency depending on the equivalent diameter and refractive index of the interacting particle.** Shown are results for a non-absorbing aerosol (left) and an absorbing one (right). The wave length of the incident light is $\lambda_{in} = 0.88$ µm in both cases. The shown diameter range corresponds to the one covered by the ELPI+-device.

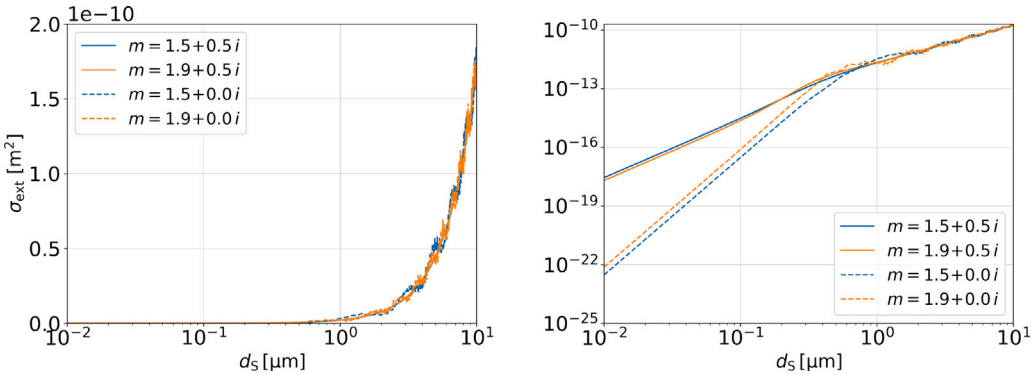


**Fig. 4. Extinction cross section of one interacting particle depending on the equivalent diameter of the particle.** Shown are results obtained from Eq. (10) for different refractive indices. Both diagrams have in fact the same content. In the right one, however, the $y$-axis has a logarithmic scale. The wave length of the incident light is again $\lambda_{in} = 0.88$ µm.

*Extinction cross section* $\sigma_{ext}$

This quantity is directly related to the extinction efficiency. In contrast to the latter, however, it is a physical observable that can actually be measured experimentally. Cross section and efficiency are related through the *visible* particle area in the direction of the light beam which is a circle in case spherical objects are considered. The extinction cross section and its constituting parts are for an equivalent particle therefore given by

$$\sigma_j(\lambda_{in}, d_S, m) := q_j(\lambda_{in}, d_S, m) \cdot \pi \cdot \left(\frac{d_S}{2}\right)^2, \qquad j \in \{ext,\ sca,\ abs\}. \tag{10}$$

Examples of extinction cross sections for different refractive indices are shown in Fig. 4. In first approximation, the distributions are monotonously increasing. Larger particles therefore have a larger extinction cross section than smaller ones. Moreover, relevant dependence on the refractive index is only present for equivalent diameters smaller than the wave length of the incident light. Particles larger than that almost behave identically which corresponds to the principles of geometrical optics [7].

*Extinction coefficient*[4] $\alpha_V$

This quantity is the cumulative sum of all particle extinction cross sections of an aerosol. Several different definitions can be found in the literature. In the present contribution, we use the so-called *volume extinction coefficient* which is normalized to unit volume $V_u = 1\,cm^3$. In this form, it is exactly the quantity that enters the Bouguer–Lambert law in Eq. (8) [7]. Using particle number densities of the 14 ELPI+-channels defined in Eq. (1a) as well as extinction cross sections given in Eq. (10), $\alpha_V$ can be written as

$$\alpha_V(t) = \sum_{i=1}^{14} \alpha_{V,i}(t) = \sum_{i=1}^{14} \frac{N_i(t)}{V_u} \cdot \sigma_{ext}(d_{S,i}, m) = \sum_{i=1}^{14} \rho_{N,i}(t) \cdot \sigma_{ext}(d_{S,i}, m) \tag{11a}$$

$$\overset{(1a),(10)}{=} \pi \sum_{i=1}^{14} q_{ext}(d_{S,i}, m) \cdot \left(\frac{d_{S,i}}{2}\right)^2 \cdot X_{N,i}(d_{S,i}) \cdot I_i(t). \tag{11b}$$

Eq. (11b) is one of the most important formulas in the present contribution. In this formula, extinction coefficients are expressed in terms of extinction efficiencies $q_{ext}$ (and therefore depend on the refractive index $m$), equivalent diameters $d_{S,i}$ (and therefore depend indirectly on corresponding particle densities $\rho_{part,i}$, see Eq. (4)), conversion factors $X_{N,i}$, and electrical currents $I_i(t)$ measured by the ELPI+-device.

In the following, we assume the same *effective* particle density $\rho_{part}$ for each ELPI+-channel,

$$\rho_{part,i} \equiv \rho_{part}, \qquad i \in \{1, \ldots, 14\}, \tag{12}$$

which turns out to be sufficient to consistently combine model predictions and experimental results from MIREX- and ELPI+-measurements.[5]

[4] In some references, this quantity is also denoted as 'attenuation' coefficient, see e. g. [7].

[5] The authors of the present contribution are aware of the fact that individual particle densities $\rho_{part,i}$ can actually be assumed to be different for individual ELPI+-channels, see e. g. [17]. We further comment on limitations of assumption (12) in the course of the contribution, in particular in Section 3.

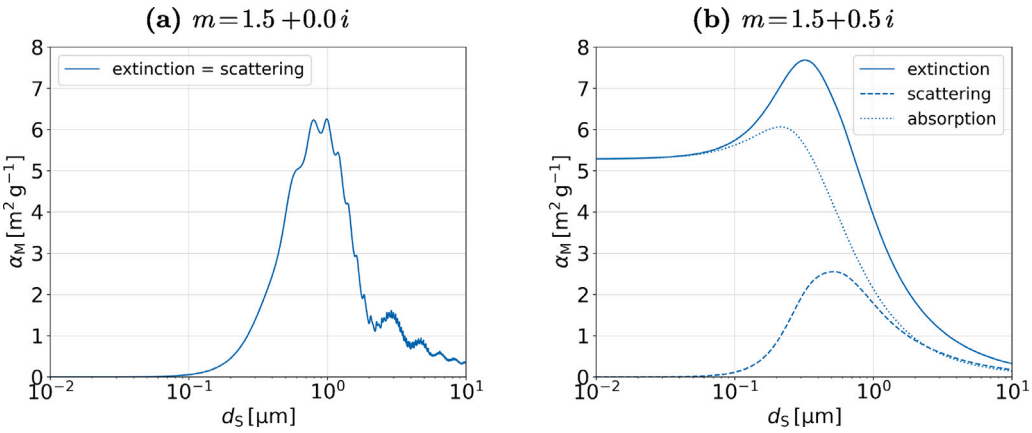


**Fig. 5. Mass-specific extinction of a single aerosol particle depending on the equivalent diameter of the particle.** The curves are obtained from Eq. (15) using $m = 1.5+0.0\,i$ (left) and $m = 1.5+0.5\,i$ (right). The particle density and the wave length of the incident light are in both cases fixed as $\rho_{\text{part}} = 1\,\text{g cm}^{-3}$ and $\lambda_{\text{in}} = 0.88\,\mu\text{m}$, respectively.

Using Eq. (12), we therefore only have *three independent aerosol properties* in Eq. (11b) that can be used to adjust the model, namely

- the real part $\Re\mathfrak{e}(m)$ of the refractive index which describes *scattering* properties of the aerosol particles,
- the imaginary part $\Im\mathfrak{m}(m)$ of the refractive index which describes *absorbing* properties of the aerosol particles, and
- the effective particle density $\rho_{\text{part}}$.

In Section 3, we consider different aerosols and show that, using known literature values of $m$ and $\rho_{\text{part}}$, it is possible to consistently describe all obtained experimental results within a unified framework. For some applications it turns out to be useful to also define the cumulative extinction coefficient obtained from the first $n$ ELPI+-channels only, similar to Eq. (6):

$$\alpha_V^{(n)}(t) := \sum_{i=1}^{n} \alpha_{V,i}(t)\,, \qquad n \in \{1, \ldots, 14\}\,. \tag{13}$$

*Mass-specific extinction coefficient* $\alpha_M$

This quantity is closely related to the extinction coefficient $\alpha_V$ and describes light extinction per mass density unit of the aerosol. According to [7], it is defined as

$$\alpha_M := \frac{\alpha_V(t)}{\rho_{\text{aerosol}}(t)}\,. \tag{14}$$

To be able to estimate the size of $\alpha_M$, we first consider a single equivalent particle and determine its contribution to the total value of $\alpha_M$. Using Eqs. (11b), (6), and (1), mass-specific extinction of a single particle associated with ELPI+-channel $i$ can be written as

$$\alpha_{M,i} := \frac{\alpha_{V,i}}{\rho_{\text{aerosol},i}} = \frac{3}{2}\frac{q_{\text{ext}}(d_{S,i}, m)}{d_{S,i} \cdot \rho_{\text{part}}}\,. \tag{15}$$

Accordingly, $\alpha_{M,i}$ is a constant in time that depends on the extinction efficiency, on the corresponding Stokes equivalent diameter (directly and indirectly), as well as on the particle density. Exemplary results for two different refractive indices are shown in Fig. 5. Since $q_{\text{ext}} \to 2$ in the limit of large (equivalent) particles, see Fig. 3, mass-specific extinction vanishes for large $d_S$:

$$\lim_{d_{S,i} \to \infty} \alpha_{M,i} = 0\,. \tag{16}$$

The reason for this effect is that $\alpha_V$ is related to the circular-shaped *surface* of the equivalent particle in the direction of the light beam (and therefore $\propto d_S^2$, see Eq. (10)), whereas $\rho_{\text{aerosol}}$ is related to the particle *volume* (and therefore $\propto d_S^3$, see Eq. (1b)). For increasing values of $d_S$, the overall dependence is therefore $\propto d_S^{-1}$. In other words, contributions to mass-specific extinction from the largest particles measured by the ELPI+-device are smaller than the ones from intermediate-size particles since larger particles proportionally contribute more to the aerosol density than to light extinction. Accordingly, $\alpha_M$ in Eq. (14) describing the whole aerosol does not depend on numerical values of $\alpha_V$ and $\rho_{\text{aerosol}}$ alone, but also on the *size-distribution* of the individual equivalent diameters. This fact is a general prediction of classical electrodynamics and already evident within the measuring range of the ELPI+-device, as can be seen in Fig. 5.

## 3. Application of the model

In the previous section, we deduce Eq. (11b) in which light-intensity reduction is expressed in terms of the parameters $m$ and $\rho_{\text{part}}$. For a given aerosol, it is in principle possible to use known literature values of the input parameters to obtain corresponding results for extinction coefficients. This, however, is complicated by the fact that both quantities are comparatively difficult to determine experimentally and, more importantly, through distinct independent measurements. Typically, the literature does therefore not provide combinations of $m$ and $\rho_{\text{part}}$ but only values or value ranges for one parameter at a time. Then, it is often not clear if considered measurements have actually been conducted under overall comparable experimental conditions.

In this contribution, we therefore follow a different approach. Since light extinction is determined independently through MIREX-measurements in each of the conducted experiments, we consider $\alpha_V(t)$ and its time average $\overline{\alpha}_V$ as known and try to reproduce obtained MIREX-results by finding appropriate combinations of $m$ and $\rho_{\text{part}}$ in Eq. (11b). We do this by scanning the refractive index over the known range of literature values. For each fixed $m$, we then successively increase the numerical value of $\rho_{\text{part}}$ unless the time average of $\alpha_V(t)$ is the same for both measurements, i. e. $\overline{\alpha}_{V,\text{ELPI+}} \equiv \overline{\alpha}_{V,\text{MIREX}}$. Although in principle all ELPI+-channels can be used in the evaluation of the measurement data, in the following we only consider the first 13 stages. This is done since contributions of channel 14 to total light extinction are only small (less than 1 % in case of paraffin and less than 5 % in case of TF5). In this way, however, the total amount and therefore the quality of valid data that can be evaluated increases significantly. In this setup, the measuring range of the ELPI+ is approximately given by $0.006\,\mu\text{m} < d_S < 4\,\mu\text{m}$.

### 3.1. Extinction coefficient $\alpha_V$

*Paraffin aerosol*

All paraffin experiments discussed in this contribution have been conducted at the department of Communication Systems at the University of Duisburg–Essen using the test duct and the AGW oil generator described in [18]. In each of the experiments, a ‘ramp’ setup is considered in which the aerosol concentration is successively increased

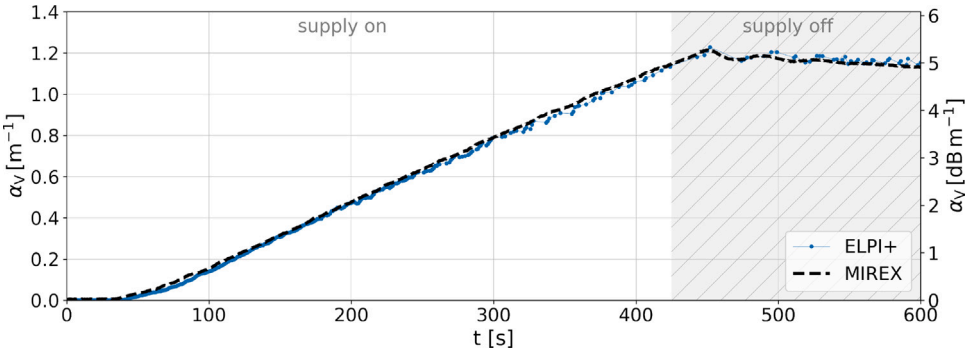


**Fig. 6. Time-dependent extinction coefficient obtained from a paraffin ramp experiment.** The black curve is obtained from the MIREX-system, the blue curve from Eq. (11b) using $m = 1.42$ and $\rho_{\mathrm{part}} = 0.85\,\mathrm{g\,cm^{-3}}$. The white area indicates the time span in which the aerosol concentration is increased by external supply. In the gray area, the supply is stopped and the system passes into a steady state. (For interpretation of the references to color in this figure legend, the reader is referred to the web version of this article.)

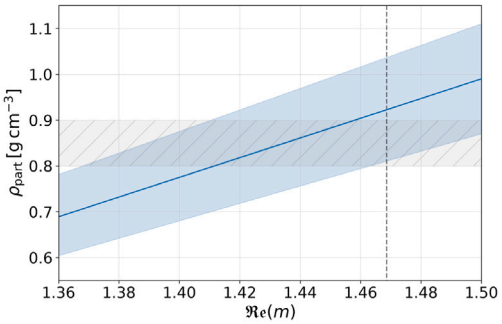


| $\Re\mathrm{e}(m)$ | $\rho_{\mathrm{part}}\,[\mathrm{g\,cm^{-3}}]$ |
|---|---|
| 1.30 | $0.56 \pm 0.06$ |
| 1.35 | $0.68 \pm 0.07$ |
| 1.40 | $0.77 \pm 0.08$ |
| 1.45 | $0.88 \pm 0.12$ |
| 1.50 | $0.99 \pm 0.13$ |

**Fig. 7. Values of $\rho_{\mathrm{part}}$ for which MIREX-and ELPI+-measurements of the paraffin aerosol agree best.** Shown is the dependence on the value of $\Re\mathrm{e}(m)$ (blue solid line and corresponding values in the table), including the $3\sigma$-range (blue band and uncertainties in the table). The grey band indicates the value range in Eq. (17c); the dashed vertical line refers to the refractive index obtained from an analytical formula provided in [21].

by external supply before the supply is stopped and a steady state is forming. As value ranges of the model parameters we consider[6]

$$\Re\mathrm{e}(m) = (1.3 - 1.5) \qquad [21\text{–}23]\,, \tag{17a}$$

$$\Im\mathrm{m}(m) = 0 \qquad [21\text{–}23]\,, \tag{17b}$$

$$\rho_{\mathrm{part}} = (0.8 - 0.9)\,\mathrm{g\,cm^{-3}}\ (\text{at } 20\,^{\circ}\mathrm{C})\,. \tag{17c}$$

Note, that the imaginary part of the refractive index vanishes. Accordingly, the aerosol does not absorb light and extinction is determined exclusively by scattering processes, see also Eq. (9).

The comparison of MIREX- and ELPI+-measurements for one exemplary paraffin ramp experiment is shown in Fig. 6. As can be seen, almost perfect agreement between the two measuring systems can be obtained using appropriate model parameters, in this case $m = 1.42$ and $\rho_{\mathrm{part}} = 0.85\,\mathrm{g\,cm^{-3}}$. It is important to emphasize that these numerical values are simultaneously compatible with the value ranges in Eqs. (17) and, therefore, with known results from the literature. This fact serves as a first indication that the developed model is able to correctly describe MIREX- and ELPI+-measurements without the need of introducing additional correction or conversion factors. Among other things, this comprises the correct description of different experimental phases ('ramp' phase, steady state) as well as subtleties in the time development of $\alpha_V$ (in Fig. 6 e. g. for times $450\,\mathrm{s} < t < 500\,\mathrm{s}$).

[6] Also smaller values of $\Re\mathrm{e}(m)$ can be found in the literature, e. g. in Refs. [19,20]. These values, however, have been obtained for larger ambient temperatures of $T_{\mathrm{exp}} \geq 40\,^{\circ}\mathrm{C}$.

It is important to notice that agreement between MIREX- and ELPI+-measurements is not only obtained for one particular combination of $m$ and $\rho_{\mathrm{part}}$ but for different ones. Considering the average of eight independent paraffin ramp experiments and scanning over the entire value range in Eq. (17a), we obtain further parameter combinations for which agreement between MIREX- and ELPI+-measurements is achieved. The results are summarized in Fig. 7. Since obtained fit values of $\rho_{\mathrm{part}}$ differ slightly from one experiment to another, particle densities are subject to small variations for which we provide the $3\sigma$-range. In general, larger values of $\Re\mathrm{e}(m)$ correspond to larger particle densities and therefore to smaller (Stokes) equivalent particles, see for instance Eq. (4). Since smaller particles correspond in first approximation to less light extinction of the aerosol (see Fig. 4), overall scattering in the presence of a paraffin aerosol therefore increases with increasing values of $\Re\mathrm{e}(m)$. In this regard, it should be noted that the blue band in Fig. 7 is simultaneously compatible with both value ranges in Eqs. (17).

Finally, we use Eq. (13) to evaluate individual contributions of the different ELPI+-channels in the left diagram of Fig. 8. As can be seen, the main part of extinction can be assigned to only a small number of neighboring ELPI+-channels.

*Soot from flaming n-heptane fire*

A second application case of the model is a room-scale setup investigating soot from flaming *n*-heptane fires (test fire TF5 according to standard EN54 [25]). The corresponding aerosol measurements of the ELPI+ were performed using a dilution system with a fixed dilution factor of 140 [13]. Further details of the experimental setup are provided in [26]. In general, the aerosol is characterized by two

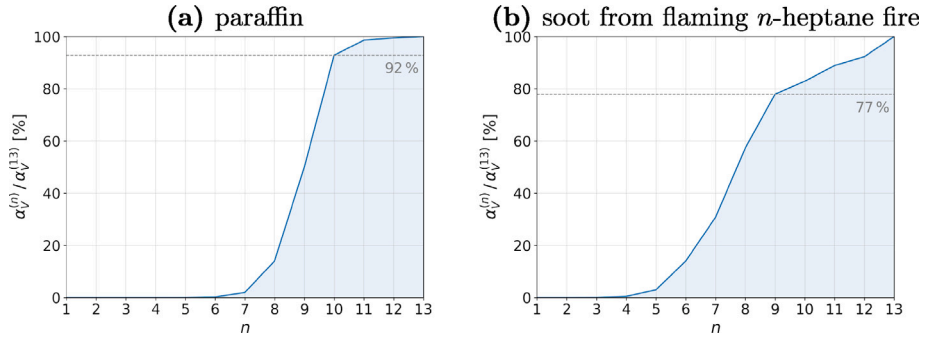


**Fig. 8. Relative cumulative contribution of the different ELPI+-channels to extinction.** Shown are results obtained from Eq. (13). In the left diagram, the first 10 channels combined contribute 92 % to entire light extinction; the main part (91 %) stems from channels 8, 9, and 10 only. In the right diagram, the first 9 channels contribute 77 % to light extinction; the main part (76 %) stems from channels 6, 7, 8, and 9.

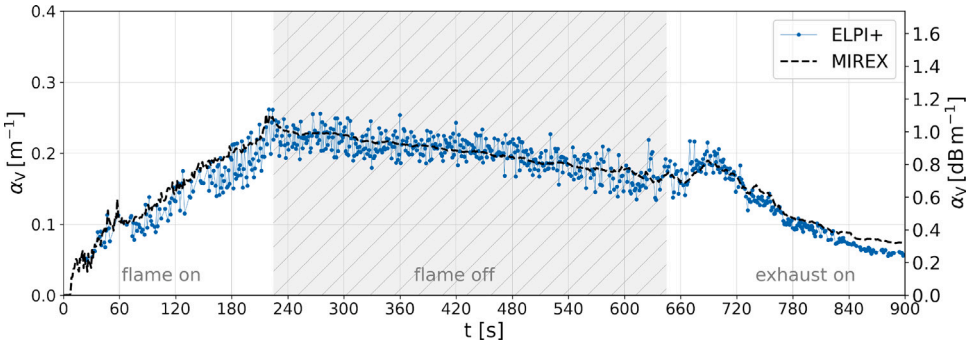


**Fig. 9. Extinction coefficient obtained from an *n*-heptane fire experiment.** The black curve is the result of the MIREX-system; the blue curve is the result of Eq. (11b) using $m = 1.57 + 0.56\,i$ and $\rho_{\text{part}} = 2.21\,\text{g cm}^{-3}$. The differently shaded areas indicate different phases of the soot generation, namely the flame-on, the flame-off, and the exhaust-on phase, respectively.

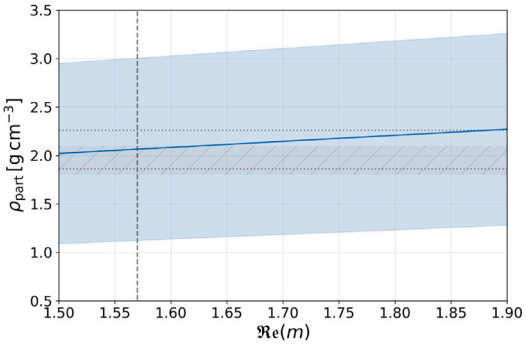


| $\mathfrak{Re}(m)$ | $\mathfrak{Im}(m)$ | $\rho_{\text{part}}\,[\text{g cm}^{-3}]$ |
|---|---|---|
| 1.50 | 0.40 | $1.80 \pm 0.28$ |
| 1.90 | 0.40 | $2.13 \pm 0.29$ |
| 1.50 | 0.50 | $2.02 \pm 0.32$ |
| 1.90 | 0.50 | $2.27 \pm 0.31$ |
| 1.57 | 0.56 | $2.18 \pm 0.35$ |
| 1.50 | 0.60 | $2.23 \pm 0.36$ |
| 1.90 | 0.60 | $2.40 \pm 0.34$ |
| 1.50 | 0.70 | $2.45 \pm 0.41$ |
| 1.90 | 0.70 | $2.53 \pm 0.37$ |

**Fig. 10. Values of $\rho_{\text{part}}$ for which MIREX-and ELPI+-results agree best.** Shown is the dependence on the values of $\mathfrak{Re}(m)$ and $\mathfrak{Im}(m)$ (blue solid line and values in the table), including the $3\sigma$-range (blue band and uncertainties in the table). In the diagram, the imaginary part of $m$ is fixed as $\mathfrak{Im}(m) = 0.5$, whereas the dashed vertical line refers to the commonly used real part $\mathfrak{Re}(m) = 1.57$ [24]. The dotted horizontal lines denote the density of crystalline graphite ($\rho_{\text{part}} = 2.26\,\text{g cm}^{-3}$) and the commonly used density for carbonaceous soot ($\rho_{\text{part}} = 1.86\,\text{g cm}^{-3}$ [8]), respectively.

major differences compared to paraffin: First, the particle density $\rho_{\text{part}}$ is *larger* than unit density $1\,\text{g cm}^{-3}$. Stokes equivalent spheres are therefore smaller than corresponding aerodynamic ones. Second, soot from an *n*-heptane fire absorbs parts of a light beam. Light extinction is therefore a combination of scattering and absorption processes and not of scattering alone, see e. g. Eq. (9). Compared to paraffin, we therefore have three independent variables instead of two:

$$\mathfrak{Re}(m) = (1.5 - 1.9) \qquad [10,24,27\text{–}29]\,, \tag{18a}$$

$$\mathfrak{Im}(m) = (0.4 - 0.7) \qquad [10,24,27\text{–}29]\,, \tag{18b}$$

$$\rho_{\text{part}} = (1.8 - 2.1)\,\text{g cm}^{-3} \quad [8,9,17,30\text{–}34]\,. \tag{18c}$$

Choosing the most commonly used refractive index for carbonaceous soot, $m = 1.57 + 0.56\,i$ (see [24] and references therein), the comparison between MIREX- and ELPI+-measurements for one exemplary experiment is shown in Fig. 9. Compared to a paraffin aerosol, the distribution is characterized by larger dynamics from one time step to another which is due to the fact that we are evaluating a room-scale experiment instead of a bench-scale one. As before, however, subtleties in the time development of $\alpha_{\text{V}}$ like different experimental

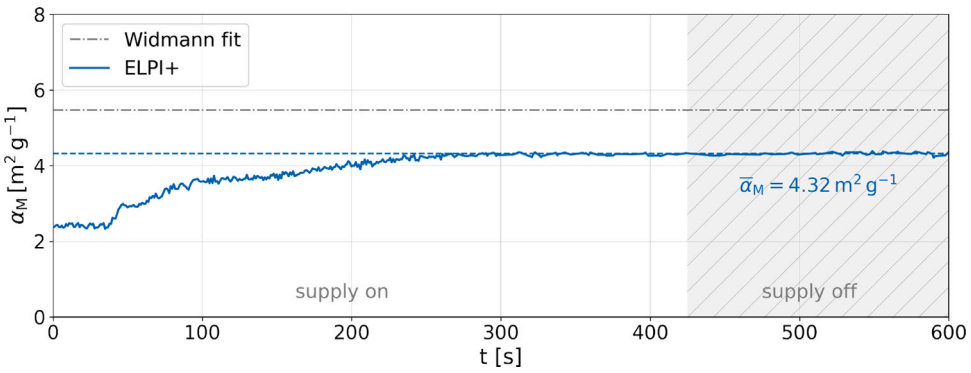


**Fig. 11. Mass-specific extinction obtained from a paraffin ramp experiment using Eq. (14).** A time average of $\overline{\alpha}_M = 4.32\,m^2\,g^{-1}$ is obtained within the supply-off phase. For the model parameters, we use the same values as in Fig. 6, namely $m = 1.42$ and $\rho_{part} = 0.85\,g\,cm^{-3}$.

phases (flame-on, flame-off, exhaust-on phase) and local extrema (in particular within the exhaust-on phase) are correctly recovered. Taking the average of the four independent *n*-heptane fire experiments in Fig. 2 and choosing exemplary values for $m$ compatible with Eqs. (18), we again obtain distinct parameter combinations for which the result of Eq. (11b) coincides with the respective MIREX-measurement, see Fig. 10. As before, particle densities increase with increasing values of $\mathfrak{Re}(m)$. However, the increase is less pronounced in general and smaller for larger values of $\mathfrak{Im}(m)$. Overall, it turns out that Eq. (11b) yields reliable results also for flaming *n*-heptane fires in a room-scale setup.

Finally, we again use Eq. (13) to evaluate individual contributions of the ELPI+-channels, see the r. h. s. of Fig. 8. Compared to paraffin, the slope of the distribution is less steep. However, the main part of extinction again stems from only a small number of neighboring channels.

### 3.2. Mass-specific extinction coefficient $\alpha_M$

In the literature, mass-specific extinction has so far has been studied empirically and mainly in small-scale experiments under well-controlled and well-ventilated conditions. A review of such results is provided e. g. in [11], finding an overall fit of the collected data as $\alpha_M = 4.8081\,m^2\,g^{-1}(\lambda_{in}/\mu m)^{-1.0088}$, depending on the wave length of the incident light. Transferred to the present MIREX-experiments ($\lambda_{in} = 0.88\,\mu m$), the fit yields

$$\alpha_M = (5.5 \pm 0.6)\,m^2\,g^{-1} \qquad (95\%\ \text{c.l.})\ [11]\,, \tag{19}$$

which is quoted to be valid (at least) for all kinds of carbonaceous soot. In the following, we test the hypothesis of a (universal) mass-specific extinction coefficient. More precisely, we first check if constant mass-specific extinction does occur at all in the conducted experiments. If so, we determine numerical values of the corresponding extinction coefficients and compare them with Eq. (19). Before starting, it should be noted that the quantities entering Eq. (14) are approximately fixed in our evaluation: On the one hand, values of $\alpha_V$ are obtained from independent MIREX-measurements and correctly described by the developed model in terms of $m$ and $\rho_{part}$. Aerosol densities $\rho_{aerosol}$, on the other hand, do not depend on $m$ and are almost independent of the particle density $\rho_{part}$ which is shown in Section 2.1. Accordingly, obtained values of $\alpha_M$ are approximately a direct output of the applied experimental and theoretical setup.

*Paraffin aerosol*

To start, we consider a paraffin ramp experiment and show results obtained from Eq. (14) in Fig. 11. First of all, it is obvious that the value of $\alpha_M(t)$ increases in the supply-on phase before it stabilizes for times $t > 300\,s$. Accordingly, a steady state regarding mass-specific extinction is indeed forming with an average value in the supply-off phase of $\overline{\alpha}_M = 4.32\,m^2\,g^{-1}$.

**Table 1**
Average $\alpha_M$-values obtained from paraffin experiments. Shown are results obtained from Eqs. (14), (11b), and (6). Given uncertainties of $\overline{\alpha}_M$ correspond to the $3\sigma$-range and include variations from one experiment to another as well as uncertainties of $\rho_{part}$.

| $\mathfrak{Re}(m)$ | $\rho_{part}\,[g\,cm^{-3}]$ | $\overline{\alpha}_M\,[m^2\,g^{-1}]$ |
|---|---|---|
| 1.30 | $0.56 \pm 0.07$ | $4.54 \pm 0.92$ |
| 1.35 | $0.68 \pm 0.07$ | $4.42 \pm 0.80$ |
| 1.40 | $0.77 \pm 0.08$ | $4.38 \pm 0.93$ |
| 1.45 | $0.88 \pm 0.12$ | $4.32 \pm 1.08$ |
| 1.50 | $0.99 \pm 0.12$ | $4.26 \pm 0.90$ |

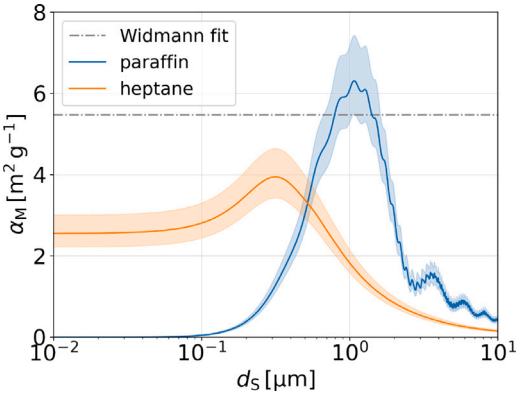


**Fig. 12. Mass-specific extinction depending on the diameter of the equivalent particle.** The curves are obtained from Eq. (15) using $m = 1.40$, $\rho_{part} = 0.77\,g\,cm^{-3}$ for paraffin and $m = 1.57 + 0.56\,i$, $\rho_{part} = 2.18\,g\,cm^{-3}$ for soot from a flaming *n*-heptane fire, respectively. These values are compatible with obtained results summarized in Figs. 7 and 10. The bands indicate a variation of $\rho_{part}$ by $\pm 15\,\%$, respectively. The wave length of the light is $\lambda_{in} = 0.88\,\mu m$.

Second, in order to check the impact of the particle density $\rho_{part}$, we consider the average of in total eight experiments as before and summarize best fit values in Table 1. As expected, the $\rho_{part}$-dependence of $\overline{\alpha}_M$ is only weak. For instance, a 77 % increase of $\rho_{part}$ in Table 1 corresponds to an $\overline{\alpha}_M$-reduction of only 6 %. Combining the results, we therefore estimate mass-specific extinction for a paraffin aerosol at a wave length of $\lambda_{in} = 0.88\,\mu m$ as

$$\alpha_M = (4.4 \pm 1.1)\,m^2\,g^{-1} \qquad (99.7\%\ \text{c.l.})\,. \tag{20}$$

Comparing the result with the literature, it is noticeable that Eq. (20) agrees with Eq. (19) within the specified uncertainties, but is in general slightly smaller. This fact, however, is compatible with fundamental

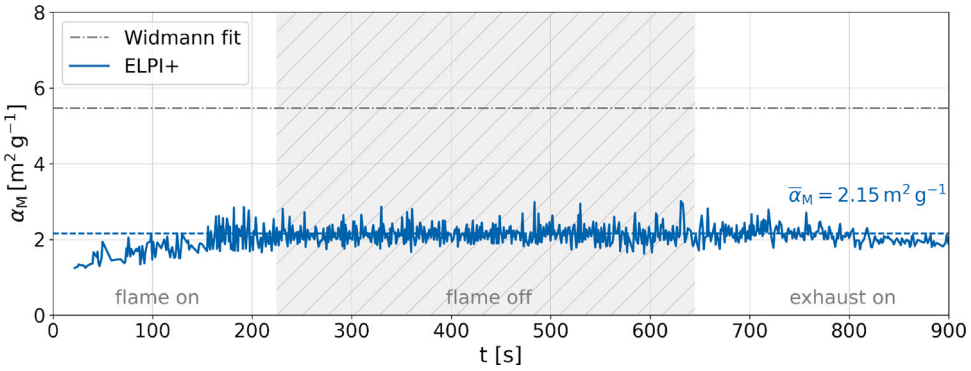


**Fig. 13. Mass-specific extinction from an *n*-heptane fire experiment using Eq. (14).** A time average of $\overline{\alpha}_M = 2.15\,m^2\,g^{-1}$ is obtained within the flame-off phase. For the model parameters, we use the same values as in Fig. 9, namely $m = 1.57 + 0.56\,i$ and $\rho_{part} = 2.21\,g\,cm^{-3}$.

**Table 2**
Average $\alpha_M$-values obtained from *n*-heptane fire experiments. Shown are results obtained from Eqs. (14), (11b), and (6). Given uncertainties of $\overline{\alpha}_M$ correspond to the $3\sigma$-range and include variations from one experiment to another as well as uncertainties of $\rho_{part}$.

| $\Re\mathfrak{e}(m)$ | $\Im\mathfrak{m}(m)$ | $\rho_{part}$ [g cm$^{-3}$] | $\overline{\alpha}_M$ [m$^2$ g$^{-1}$] |
|---|---|---|---|
| 1.50 | 0.40 | $1.80 \pm 0.28$ | $2.38 \pm 0.96$ |
| 1.90 | 0.40 | $2.13 \pm 0.29$ | $2.38 \pm 1.02$ |
| 1.50 | 0.50 | $2.02 \pm 0.32$ | $2.37 \pm 0.96$ |
| 1.90 | 0.50 | $2.27 \pm 0.31$ | $2.38 \pm 0.99$ |
| 1.57 | 0.56 | $2.18 \pm 0.35$ | $2.38 \pm 1.00$ |
| 1.50 | 0.60 | $2.23 \pm 0.36$ | $2.38 \pm 0.98$ |
| 1.90 | 0.60 | $2.40 \pm 0.34$ | $2.38 \pm 1.01$ |
| 1.50 | 0.70 | $2.45 \pm 0.41$ | $2.38 \pm 1.01$ |
| 1.90 | 0.70 | $2.53 \pm 0.37$ | $2.38 \pm 1.02$ |

predictions of Mie theory, which can be seen for instance in Fig. 12. Only within a small range of $d_S$ is it *at all* possible to obtain values equal to or larger than $\alpha_M = 5.5\,m^2\,g^{-1}$, e. g. for $d_S \approx 1\,\mu m$ (blue curve). Since the considered aerosol is made of particles that differ in their individual aerodynamic and gravimetric properties (and therefore in corresponding equivalent diameters $d_S$), average values of $\alpha_M$ can indeed be expected to be smaller than the *maximum possible* value of the distribution. This is true despite the fact that the $d_S$-distribution of a paraffin aerosol is comparatively narrow, see for instance the left diagram in Fig. 8.

*Soot from flaming n-heptane fire*

To study mass-specific extinction for soot from a flaming *n*-heptane fire, we apply the same setup as for the paraffin aerosol. Corresponding results are summarized in Table 2 and Fig. 13. As for paraffin, a steady state with constant average values of $\alpha_M$ is forming in Fig. 13. Moreover, almost all $\overline{\alpha}_M$-values in Table 2 are identical, irrespective of the actual values of $m$ and $\rho_{part}$. We therefore estimate mass-specific extinction for soot from flaming *n*-heptane fires as

$$\alpha_M = (2.4 \pm 1.8)\,m^2\,g^{-1} \qquad (99.7\%\,\text{c.l.}), \tag{21}$$

considering again particle sizes between $d_S = 0.006\,\mu m$ and $d_S \approx 4\,\mu m$ as well as $\lambda_{in} = 0.88\,\mu m$.

In the assessment of the result, the following points should be noted: First, the obtained value is significantly smaller than the value in Eq. (19) and even outside the provided uncertainties. One possible reason for the deviation may be related to the dilution process which is part of the considered *n*-heptane measurements. The procedure itself is standardized and, of course, reproducible [13]. A different weighting of the various channels or a change in the overall efficiency, however, cannot be completely ruled out. In order to conservatively take into account effects caused by the dilution process as a whole, we added an additional uncertainty of 30 % to the values of $\alpha_M$ in Eq. (21). Another reason for the deviation observed could be assumed in the fact that aerosol measurements with the ELPI+ are to some extend local ones whereas MIREX-measurements are made along a one meter path in our case (although both system have been installed directly next to each other and at the same measuring height). The influence of this fact on final numerical results, however, can be estimated as low for the following reasons: First, a qualitative analysis in Ref. [26] supports the hypothesis of homogeneous horizontal smoke stratification in the considered experiments. For this reason, the measuring height is far more important than the exact horizontal measuring location in the room. Secondly, in particular the flame-off phases in the heptane-fire experiments cover a time span of more than seven minutes in each conducted experiment, see for instance Fig. 13. Any inhomogeneities or residual thermals that may be still there immediately after the flame-on phase are therefore likely to average out during the comparatively long steady-state period.

Apart from this, discrepancies towards the referenced literature value similar to the one in Eq. (21) are reproduced within the scope of a study that has been conducted recently [26]. Here, the setup of the experiment was mapped by a numerical CFD model assuming a mass-specific extinction coefficient as defined in Eq. (14). Local optical measurements with the MIREX-device revealed an overestimation of the computed extinction coefficient by a factor of approximately four. This result is compatible with Eq. (21) if one compares it with the default value of $\alpha_M = 8.7\,m^2\,g^{-1}$ used in the simulations [6,12]. On a spatial and temporal scale, the deviation showed an almost linear correlation over the entire duration of the fire. Finally, Eq. (21) is also compatible with [10] when using it to compute the corresponding *dimensionless* extinction coefficient $K_e$, see Table 4 in Appendix A.2.

From the model point of view, the fact that the result in Eq. (21) is smaller than the one in Eq. (20) is actually compatible with predictions of Mie theory, see Fig. 12. At first glance, it is obvious that the *maximum possible* value of $\alpha_M$ is considerably smaller in case of heptane. Moreover, for larger $d_S$, $\alpha_M$ approaches zero more quickly. Since convolution with the actual size-distribution of the aerosol particles does not change this fact, a smaller average of $\alpha_M$ is the consequence. The observations made are underpinned by the fact that the average of $\alpha_M$ increases if one only considers ELPI+-channels associated with small and intermediate-size particles. For instance, considering only the first ten ELPI+-channels (which still provide $\approx 80\,\%$ of total light extinction, see the r. h. s. of Fig. 8) and using the most commonly used particle density $\rho_{part} = 1.86\,g\,cm^{-3}$ [8], mass-specific extinction increases to $\alpha_M = (3.8 \pm 1.3)\,m^2\,g^{-1}$. This value corresponds to a smaller measuring range of the ELPI+-device as it is the average for equivalent particles up to a size of $d_S \approx 1\,\mu m$. In this case, $\alpha_M$ is still slightly smaller than the value in Eq. (19), but approaches the order of magnitude of the fit result.

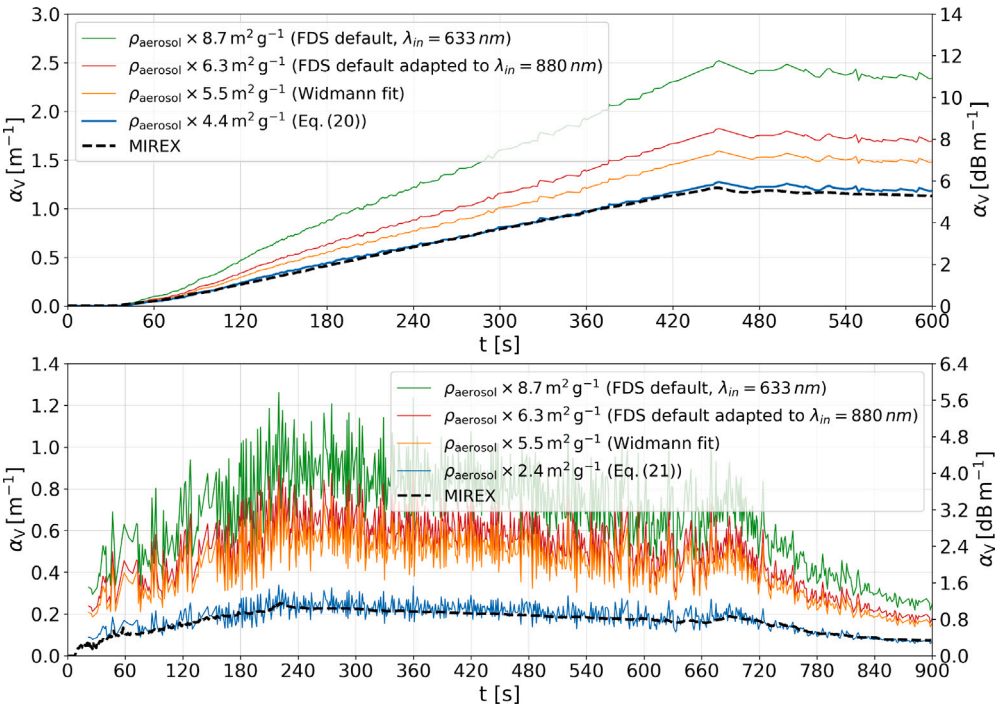


**Fig. 14. Extinction coefficient $\alpha_V$ obtained from Eq. (22).** Shown are results for a paraffin aerosol (upper diagram) and soot from a flaming *n*-heptane fire (lower diagram). In both diagrams, the particle density is set to $\rho_{part} = 1\,g\,cm^{-3}$.

### 3.3. Light extinction from future ELPI+-measurements

Now that values of $\alpha_M$ are obtained for the considered aerosols, the results can be used to determine visibility conditions in future applications of the ELPI+-system or measuring devices that work in a similar way. This can be done by reversing the logic that has been used to determine $\alpha_M$-values in the first place. For this, we rewrite Eq. (14) as

$$\alpha_V(t) = \alpha_M \cdot \rho_{aerosol}(t)\,. \tag{22}$$

Accordingly, the only quantity that has to be extracted from ELPI+-data in future applications is the overall mass density of the aerosol under investigation, e. g. via Eq. (6). Multiplication with $\alpha_M$ then yields results of $\alpha_V$ which can ultimately be used in the Bouguer–Lambert law in Eq. (8).

In general, the determination of $\rho_{aerosol}$ from ELPI+-data is comparatively simple since it is approximately a direct output of the device, see e. g. Eq. (6) and the discussion below that equation. Moreover, since $\rho_{aerosol}$ is almost independent of $\rho_{part}$, it is even possible to assume $\rho_{part} = 1\,g\,cm^{-3}$ in the determination of the aerosol density.[7] Therefore, the value of $\rho_{part}$ does not necessarily have to be known when using Eq. (22).

In Fig. 14, we show results obtained using this approach.[8] As can be seen, Prediction (22) agrees much better with MIREX-results when using $\alpha_M$-values obtained in Eqs. (20) and (21) instead of Eq. (19). Moreover, the FDS default $\alpha_M = 8.7\,m^2\,g^{-1}$ (valid for $\lambda_{in} = 0.633\,\mu m$ [6,12]), and the value $\alpha_M = 6.3\,m^2\,g^{-1} = 8.7\,m^2\,g^{-1} \times 0.633\,\mu m/0.88\,\mu m$ (adapted from the FDS default by assuming a functional dependence on $\lambda_{in}$ as proposed in [11]) lead to an overestimation of light extinction of in part more than a factor of three.

[7] In fact, this corresponds to using aerodynamic equivalent particles in the determination of $\rho_{aerosol}$.

[8] The experiments have been considered before in Figs. 6 and 9, and serve here as application examples.

## 4. Conclusions and outlook

In this contribution, we develop and apply a model describing light extinction in the presence of arbitrary aerosols. We do this by combining aerosol measurements performed with the cascade impactor ELPI+ and light-intensity reduction measurements performed with the extinction measuring equipment MIREX. A main motivation in developing the model was that it should yield reliable predictions of visibility conditions, but should at the same time be as simple as possible. Accordingly, several assumptions were made in order to focus on most relevant characteristics of the aerosol. This results in the fact that model predictions essentially depend on only three independent parameters: the effective particle density $\rho_{part}$ as well as real and imaginary parts of the refractive index $m$. Despite the strong restrictions, Eq. (11b) is able to correctly describe time-dependent light extinction in the presence of an arbitrary aerosol. This comprises, among other things, different phases of the aerosol generation (flame-on, flame-off, exhaust-on phase) as well as other experimental conditions (bench scale and room scale, ventilation conditions, etc.). As it turns out, valid values of the input parameters $\rho_{part}$, $\Re\epsilon(m)$, and $\Im m(m)$ are simultaneously compatible with well-established value ranges found in the literature.

The reason why the model works so well is that the ELPI+ internally maps all measured aerosol particles to spherical surrogates, no matter what shape they have. Therefore, the contribution of each sphere to overall light extinction can be estimated in the framework of Mie theory. The conversion itself is based on physical properties of the measured particles and takes into account their surface area (via the working principle of the corona charger) as well as their inertial mass, size, and shape (via the working principle of the cascade impactor). This fact can be capitalized on especially when Stokes equivalent spheres are used in the evaluation of measurement data since in this case, equivalent spheres have a size compatible with the size of the actual aerosol particles. In this way, the combination of ELPI+-data and developed model is able to correctly take into account large hierarchies of magnitudes which range for individual cross sections from $\mathcal{O}(\sigma_{ext}) = 10^{-22}\,m^2$ for the smallest particles up to $\mathcal{O}(\sigma_{ext}) = 10^{-10}\,m^2$ for the largest particles. In doing so, the model gets by without the need of introducing

additional 'correction' or 'conversion' factors and correctly predicts extinction coefficients that are typically in the order $\mathcal{O}(\alpha_V) = 1\,\mathrm{m}^{-1}$.

As a first application of the developed model, it is found that main contributions to extinction stem from only a small number of neighboring ELPI+-channels that correspond to intermediate-size particles. More precisely, for a paraffin aerosol, more than 90 % of extinction originate from only three ELPI+-channels, whereas for soot from a flaming *n*-heptane fire, ≈ 80 % of extinction stem from only four channels. This is one of the main reasons, why the concept of a *universal* particle density (which is considered to be the same for each ELPI+-channel) works at all and why valid numerical values are close to known literature values. In a second application, we verify the existence of constant mass-specific extinction, at least for the two considered aerosols. For them, we get the following results which are valid for the wave length $\lambda_{in} = 0.88\,\mu\mathrm{m}$ using the first 13 channels of the ELPI+-device (particle sizes between $d_S = 0.006\,\mu\mathrm{m}$ and $d_S \approx 4\,\mu\mathrm{m}$):

$$\textbf{paraffin aerosol}: \quad \alpha_M = (4.4 \pm 1.1)\,\mathrm{m}^2\,\mathrm{g}^{-1} \quad (99.7\%\,\mathrm{c.l.}), \tag{23a}$$

$$\textbf{soot from flaming } n\textbf{-heptane fire}: \quad \alpha_M = (2.4 \pm 1.8)\,\mathrm{m}^2\,\mathrm{g}^{-1} \quad (99.7\%\,\mathrm{c.l.}). \tag{23b}$$

The results are not universal in the sense that they have the same numerical value irrespective of the present aerosol. It is important to note, however, that this is not a drawback. On the contrary, each of the values rather considers specific aerosol characteristics that are relevant regarding light extinction, in particular size-distributions and value ranges of the equivalent particles. Therefore, Eqs. (23) can ultimately be used to reliably predict visibility conditions in future applications of the ELPI+-device. For this, it is sufficient to determine aerosol densities $\rho^{(13)}_{\mathrm{aerosol}}$ via Eq. (6) and to multiply them with the respective value of $\alpha_M$.

Finally, it should be stressed that the value for *n*-heptane in Eq. (23b) is obtained from a setup that uses the dilution system of the ELPI+. Although the dilution procedure itself is standardized and in principle well understood [13], it cannot be completely ruled out that it had an influence on the numerical result in Eq. (23b). Despite the fact that corresponding uncertainties are already taken into account in the error of Eq. (23b), future undiluted measurements should provide clarity in this regard. Beyond that, it should also be clarified to what extent the results in Eqs. (23) are valid for measurements of the aerosol density that are based on devices other than the ELPI+. Like the determination of $\alpha_M$-values describing further aerosols and the investigation of their wave-length dependence, however, these aspects are beyond the scope of the present contribution. This work is therefore left for future investigations.

## CRediT authorship contribution statement

**Christoph Gnendiger:** Conceptualization, Data curation, Formal analysis, Investigation, Methodology, Software, Validation, Visualization, Writing – original draft, Writing – review & editing. **Thorsten Schultze:** Conceptualization, Data curation, Investigation, Methodology, Writing – review & editing. **Kristian Börger:** Conceptualization, Data curation, Investigation, Writing – review & editing. **Alexander Belt:** Conceptualization, Data curation, Investigation, Writing – review & editing. **Lukas Arnold:** Conceptualization, Funding acquisition, Methodology, Project administration, Resources, Software, Supervision, Validation, Writing – review & editing.

## Declaration of competing interest

The authors declare that they have no known competing financial interests or personal relationships that could have appeared to influence the work reported in this paper.

## Data availability

Data will be made available on request.

**Table 3**
$K_e$-values obtained for a paraffin aerosol.

| $\Re\mathfrak{e}(m)$ | $\rho_{\mathrm{part}}$ [g cm$^{-3}$] | $\alpha_M$ [m$^2$ g$^{-1}$] | $K_e$ [1] |
|---|---|---|---|
| 1.35 | 0.68 | 4.42 | 2.6 |
| 1.40 | 0.77 | 4.38 | 3.0 |
| 1.45 | 0.88 | 4.32 | 3.3 |
| 1.50 | 0.99 | 4.26 | 3.7 |

**Table 4**
$K_e$-values obtained for soot from a flaming *n*-heptane fire.

| $\Re\mathfrak{e}(m)$ | $\Im\mathfrak{m}(m)$ | $\rho_{\mathrm{part}}$ [g cm$^{-3}$] | $\alpha_M$ [m$^2$ g$^{-1}$] | $K_e$ [1] |
|---|---|---|---|---|
| 1.50 | 0.40 | 1.80 | 2.38 | 3.8 |
| 1.90 | 0.40 | 2.13 | 2.39 | 4.5 |
| 1.50 | 0.50 | 2.02 | 2.37 | 4.6 |
| 1.90 | 0.50 | 2.27 | 2.38 | 4.8 |
| 1.57 | 0.56 | 2.18 | 2.38 | 4.6 |
| 1.50 | 0.60 | 2.23 | 2.38 | 4.7 |
| 1.90 | 0.60 | 2.40 | 2.38 | 5.0 |
| 1.50 | 0.70 | 2.45 | 2.38 | 5.1 |
| 1.90 | 0.70 | 2.53 | 2.38 | 5.3 |

## Acknowledgments

We would like to thank Alica Kandler from the Institute for Advanced Simulation, Forschungszentrum Jülich, for active support in the implementation of the aerosol measurements. Parts of the present contribution are funded by Deutsche Forschungsgemeinschaft (DFG, German Research Foundation) under the project number 465392452.

## Appendix

### A.1. ELPI+ conversion factors

According to [13], ELPI+ conversion factors are given by

$$X_N = \frac{1}{1.8300} \cdot \frac{J_{\mathrm{cal}}}{J_{\mathrm{imp}}} \cdot X_{\mathrm{dil}} \cdot \left(\frac{1}{d_S}\right)^{1.225}, \qquad d_S < 1.035\,\mu\mathrm{m}, \tag{24a}$$

$$X_N = \frac{1}{1.8114} \cdot \frac{J_{\mathrm{cal}}}{J_{\mathrm{imp}}} \cdot X_{\mathrm{dil}} \cdot \left(\frac{1}{d_S}\right)^{1.515}, \qquad 1.035\,\mathrm{nm} < d_S < 4.282\,\mu\mathrm{m}, \tag{24b}$$

$$X_N = \frac{1}{3.3868} \cdot \frac{J_{\mathrm{cal}}}{J_{\mathrm{imp}}} \cdot X_{\mathrm{dil}} \cdot \left(\frac{1}{d_S}\right)^{1.085}, \qquad d_S > 4.282\,\mu\mathrm{m}, \tag{24c}$$

where $J_{\mathrm{cal}}$, $J_{\mathrm{imp}}$, and $X_{\mathrm{dil}}$ denote the calibration flow rate, the impactor flow rate, and the dilution factor that can be adjusted for each ELPI+-measurement, respectively.

### A.2. Dimensionless extinction coefficient $K_e$

In the already mentioned review [11] summarizing mass-specific extinction coefficients obtained in various small-scale-experiments, the wave-length dependence of $\alpha_M$ is approximately fitted as $\alpha_M \sim \lambda_{in}^{-1}$. Assuming such a functional dependence, it is possible to define a *dimensionless* extinction coefficient $K_e$ in the following way:

$$K_e = \alpha_M \cdot \rho_{\mathrm{part}} \cdot \lambda_{in}. \tag{25}$$

Written in terms of $K_e$, the Bouguer-Lambert law in Eq. (8) is then given by

$$\frac{I(t)}{I_0} = \exp\left[-\alpha_V \cdot l\right] = \exp\left[-\alpha_M \cdot \rho_{\mathrm{aerosol}} \cdot l\right] = \exp\left[-K_e \cdot \frac{\rho_{\mathrm{aerosol}}}{\rho_{\mathrm{part}}} \cdot \frac{l}{\lambda_{in}}\right]. \tag{26}$$

Using results obtained in Sections 3.1 and 3.2, values of $K_e$ for a paraffin aerosol and soot from a flaming *n*-heptane fire are summarized in Tables 3 and 4, respectively.

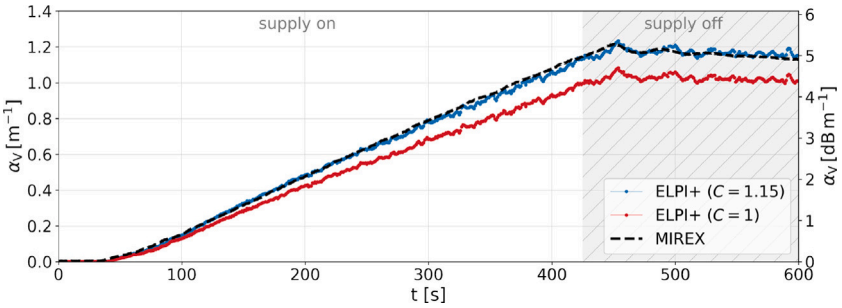


**Fig. 15. Extinction coefficient obtained when using aerodynamic equivalent spheres.** The value of $m$ is the same as in Fig. 6. The red curve is obtained without correction factor, whereas the blue curve is the result of multiplying $C = 1.15$. (For interpretation of the references to color in this figure legend, the reader is referred to the web version of this article.)

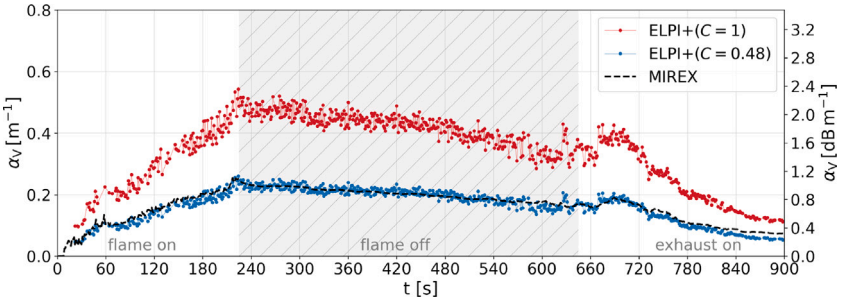


**Fig. 16. Extinction coefficient obtained when using aerodynamic equivalent spheres.** The value of $m$ is the same as in Fig. 9. The red curve is obtained without correction factor, the blue curve is the result of multiplying $C = 0.48$. (For interpretation of the references to color in this figure legend, the reader is referred to the web version of this article.)

**Table 5**
$C$-factors for a paraffin aerosol.

| $\mathfrak{Re}(m)$ | 1.30 | 1.35 | 1.40 | 1.42 | 1.45 | 1.50 |
|---|---|---|---|---|---|---|
| $\rho_{\text{part}}$ [g cm$^{-3}$] | 0.58 | 0.70 | 0.80 | 0.85 | 0.92 | 1.03 |
| $C$ | 1.70 | 1.41 | 1.21 | 1.15 | 1.07 | 0.98 |

### A.3. Aerodynamic equivalent diameters

In Section 2.1 it is shown that Stokes equivalent diameters are better suited for describing light interaction of aerosol particles than aerodynamic ones. In the following, we explicitly verify and quantify this fact by introducing a corresponding conversion factor

$$C(\rho_{\text{part}}) = \frac{\alpha_{\text{V, Stokes}}(\rho_{\text{part}})}{\alpha_{\text{V, aerodynamic}}} \equiv \frac{\alpha_{\text{V, Stokes}}(\rho_{\text{part}})}{\alpha_{\text{V, Stokes}}(\rho_{\text{part}} = 1\,\text{g cm}^{-3})}\,. \tag{27}$$

It is important to notice that, since Stokes diameters depend on the particle density $\rho_{\text{part}}$, this is of course also the case for values of $C$.

*Paraffin aerosol*

Since $\rho_{\text{part}}$ is *smaller* than $1\,\text{g cm}^{-3}$, Stokes equivalent diameters are *larger* than corresponding aerodynamic ones. For given values of $m$ and $\rho_{\text{part}}$, extinction is therefore smaller when using aerodynamic equivalent spheres which can be seen in Fig. 15. Agreement with MIREX-results can be obtained introducing correction factors $C$ as defined in Eq. (27). $C$-factors for different values of $m$ (and therefore $\rho_{\text{part}}$) are summarized in Table 5.

*Soot from flaming n-heptane fire*

Since $\rho_{\text{part}}$ is *larger* than $1\,\text{g cm}^{-3}$, Stokes equivalent diameters are *smaller* than corresponding aerodynamic ones. For given values of $\rho_{\text{part}}$ and $m$, extinction is therefore *larger* when using aerodynamic equivalent spheres which can be seen in Fig. 16. Agreement with the MIREX-measurement can be obtained when using the overall correction factors summarized in Table 6.

**Table 6**
$C$-factors for soot from a flaming $n$-heptane fire.

| $\mathfrak{Re}(m)$ | $\mathfrak{Im}(m)$ | $\rho_{\text{part}}$ [g cm$^{-3}$] | $C$ |
|---|---|---|---|
| 1.50 | 0.40 | 1.80 | 0.57 |
| 1.90 | 0.40 | 2.13 | 0.46 |
| 1.50 | 0.50 | 2.02 | 0.52 |
| 1.90 | 0.50 | 2.27 | 0.44 |
| 1.57 | 0.56 | 2.18 | 0.48 |
| 1.50 | 0.60 | 2.23 | 0.48 |
| 1.90 | 0.60 | 2.40 | 0.42 |
| 1.50 | 0.70 | 2.45 | 0.45 |
| 1.90 | 0.70 | 2.53 | 0.41 |

## References

[1] T. Jin, Visibility through Fire Smoke (I), Bull. Japan Assoc. Fire Sci. Eng. 19 (2) (1970) 1–8.
[2] T. Jin, Visibility through Fire Smoke (II), Bull. Japan Assoc. Fire Sci. Eng. 21 (1,1) (1971) 17–23.
[3] T. Jin, Visibility through Fire Smoke (III), Bull. Japan Assoc. Fire Sci. Eng. 22 (1,2) (1972) 11–15.
[4] T. Jin, Visibility through Fire Smoke (IV), Bull. Japan Assoc. Fire Sci. Eng. 23 (1,2) (1973) 1–8.
[5] T. Jin, Visibility through fire smoke, J. Fire Flammabil. 9 (1978) 135–155.
[6] K. McGrattan, R. McDermott, C. Weinschenk, G. Forney, Fire Dynamics Simulator Users Guide, sixth ed., 2022.
[7] C.F. Bohren, E. Clothiaux, D.R. Huffman, Absorption and Scattering of Light By Small Particles, Wiley-VCH, Weinheim, Bergstr, 2009.
[8] R.A. Dobbins, G.W. Mulholland, N.P. Bryner, Comparison of a fractal smoke optics model with light extinction measurements, Atmos. Environ. 28 (1994) 889–897.
[9] J.F. Widmann, J.-C. Yang, T.J. Smith, S.L. Manzello, G.W. Mulholland, Measurement of the optical extinction coefficients of post-flame soot in the infrared, Combust. Flame 134 (2003) 119–129.
[10] J.-S. Wu, S.S. Krishnan, G.M. Faeth, Refractive indices at visible wavelengths of soot emitted from buoyant turbulent diffusion flames, J. Heat Transfer 119 (2) (1997) 230–237.

[11] J. Widmann, Evaluation of the planck mean absorption coefficients for radiation transport through smoke, Combust. Sci. Technol. 175 (2003) 2299–2308.
[12] G.W. Mulholland, C. Croarkin, Specific extinction coefficient of flame generated smoke, Fire Mater. 24 (5) (2000) 227–230.
[13] Dekati Ltd, ELPI+ User manual, 2011.
[14] Cerberus Ltd, Extinction measuring equipment MIREX. Technical description, 1991.
[15] A. Järvinen, M. Aitomaa, A. Rostedt, J. Keskinen, J. Yli-Ojanperä, Calibration of the new electrical low pressure impactor (ELPI+), J. Aerosol Sci. 69 (2013).
[16] P. Laven, MiePlot, 2021.
[17] N. Coudray, A. Dieterlen, E. Roth, G. Trouvé, Density measurement of fine aerosol fractions from wood combustion sources using ELPI distributions and image processing techniques, Fuel 88 (5) (2009) 947–954.
[18] U. Müller, O. Linden, I. Willms, W. Krüll, Test duct for multi sensor fire detectors, 2004.
[19] M. Ma, Q. Ai, M. Xie, Optical properties of four types paraffin, Optik 249 (2022) 168277.
[20] D. Zhao, G. Zhang, X. Zhang, D. Li, Optical properties of paraffin at temperature range from 40 to 80 °C, Optik 157 (2018) 184–189.
[21] P.R. Cooper, Refractive-index measurements of paraffin, a silicone elastomer, and an epoxy resin over the 500–1500-nm spectral range, Appl. Opt. 21 (19) (1982) 3413–3415.
[22] D. Li, Y. Zheng, Z. Li, H. Qi, Optical properties of a liquid paraffin-filled double glazing unit, Energy Build. 108 (2015) 381–386.
[23] M. Köntges, H. Schulte-Huxel, S. Blankemeyer, M.R. Vogt, H. Holst, R. Reineke-Koch, R. Witteck, R. Brendel, Method to measure light recovery probability of pv module backsheets enabling 20.2% module efficiency with passivated emitter and rear solar cells, 2016.
[24] K.C. Smyth, C.R. Shaddix, The elusive history of m=1.57–0.56i for the refractive index of soot, Combust. Flame 107 (3) (1996) 314–320.
[25] European Committee for Standardization, EN 54-7 Fire detection and fire alarm systems — Part 7: Smoke detectors — Point detectors using scattered light, transmitted light or ionization, 2002.
[26] K. Börger, A. Belt, A. Kandler, T. Schultze, L. Arnold, Investigation of smoke characteristics by photometric measurements, in: Fire and Evacuation Modeling Technical Conference (FEMTC) 2022, 2022.
[27] C.M. Sorensen, Light scattering by fractal aggregates: A review, Aerosol Sci. Technol. 35 (2) (2001) 648–687.
[28] H. Chang, T. Charalampopoulos, Determination of the wavelength dependence of refractive indices of flame soot, Proc. R. Soc. Lond. Ser. A 430 (1880) (1990) 577–591.
[29] W.H. Dalzell, A.F. Sarofim, Optical constants of soot and their application to heat-flux calculations, J. Heat Transfer 91 (1) (1969) 100–104.
[30] M.L. Botero, N. Eaves, J.A. Dreyer, Y. Sheng, J. Akroyd, W. Yang, M. Kraft, Experimental and numerical study of the evolution of soot primary particles in a diffusion flame, Proc. Combust. Inst. 37 (2) (2019) 2047–2055.
[31] J. Slowik, E. Cross, J.-H. Han, P. Davidovcits, T. Onasch, J. Jayne, L. Williams, M. Canagaratna, D. Worsnop, R. Chakrabarty, H. Moosmuller, W. Arnott, J. Schwarz, R.-S. Gao, D. Fahey, G. Kok, A. Petzold, An inter-comparison of instruments measuring black carbon content of soot particles, Aerosol Sci. Technol. 41 (2007) 295–314.
[32] J. Schneider, S. Weimer, F. Drewnick, S. Borrmann, G. Helas, P. Gwaze, O. Schmid, M. Andreae, U. Kirchner, Mass spectrometric analysis and aerodynamic properties of various types of combustion-related aerosol particles, Int. J. Mass Spectrom. 258 (1) (2006) 37–49, Aerosols/Microparticles Special Issue.
[33] K. Park, D.B. Kittelson, M.R. Zachariah, P.H. Mcmurry, Measurement of inherent material density of nanoparticle agglomerates, J. Nanoparticle Res. 6 (2004) 267–272.
[34] C. Hueglin, C. Gaegauf, S. Künzel, H. Burtscher, Characterization of wood combustion particles: Morphology, mobility, and photoelectric activity, Environ. Sci. Technol. 31 (12) (1997) 3439–3447.